Characterization methods for strain induced damage in polypropylene

Johannes Wiener, Florian Preissegger, Bernhard Plank, Florian Arbeiter, Otmar Kolednik, Gerald Pinter

Angaben zur Veröffentlichung / Publication details:

Wiener, Johannes, Florian Preissegger, Bernhard Plank, Florian Arbeiter, Otmar Kolednik, and Gerald Pinter. 2022. "Characterization methods for strain induced damage in polypropylene." *Polymer Engineering & Science* 62 (6): 1959–73. https://doi.org/10.1002/pen.25979.

Received: 24 January 2022 | Revised: 21 March 2022 | Accepted: 21 March 2022

DOI: 10.1002/pen.25979

RESEARCH ARTICLE

POLYMER ENGINEERING AND SCIENCE WILEY

Characterization methods for strain-induced damage in polypropylene

Johannes Wiener[1] | **Florian Preissegger**[1] | **Bernhard Plank**[2,3] | **Florian Arbeiter**[1] | **Otmar Kolednik**[4] | **Gerald Pinter**[1]

[1]Materials Science and Testing of Polymers, Montanuniversitaet Leoben, Leoben, Austria

[2]Research Group Computed Tomography, University of Applied Sciences Upper Austria: Campus Wels, Wels, Austria

[3]Mechanical Engineering, University of Augsburg, Augsburg, Germany

[4]Erich-Schmid-Institute of Materials Science, Austrian Academy of Science, Leoben, Austria

Correspondence
Florian Arbeiter, Materials Science and Testing of Polymers, Montanuniversitaet Leoben, 8700 Leoben, Austria.
Email: florian.arbeiter@unileoben.ac.at

Funding information
State Government of Upper Austria; pore3D, Grant/Award Number: 868735; BeyondInspection, Grant/Award Number: 874540; Austrian Research Promotion Agency (FFG), Grant/Award Number: 858562

Abstract

Various methods are used to characterize the deterioration of mechanical properties in polymers. The focus is set on distinguishing between time-dependent and irreversible damage in two different grades of polypropylene. First, digital image correlation is utilized to capture the stress–strain behavior during monotonic tensile tests. Changes in specimen volume are recorded throughout the experiment and serve as an indicator for crazes and voids. However, the elastic modulus, E, cannot be monitored throughout the entire experiment. Further analysis is performed in the form of cyclic load–unload tests. E and the residual strain, ε_{res}, as a function of the applied strain, ε_{appl}, are obtained for each cycle. Results show that E primarily suffers from the time-dependent behavior of the tested polymers in this case. Subsequently, an alternative technique is applied, where specimens are prestrained and then allowed to relax. In the following dynamic mechanical analysis, viscoelastic effects can be avoided. Considerations on the onset and evolution of damage are made. Ultimately, these results are confirmed through microcomputed tomography, where the shapes and densities of defects are captured in high resolution.

KEYWORDS

computed tomography, damage, elastic modulus decay, polypropylene

1 | INTRODUCTION

Various mechanisms of microstructural damage are known in literature. Unfortunately, the definitions and descriptions often vary. For the purposes of this contribution, the focus is set on four closely related types of microstructural damage, namely voids, microcracks, polar fans, and crazes (Figure 1A–D). Voids are defects with no characteristic shape or orientation and often act as starting point for material failure. In homogeneous materials, void growth starts from local irregularities in the molecular packing.[1] In heterogeneous materials, voids can initiate from rubber particles[2] or reinforcing particles.[3,4] In these examples, the debonding of particles from the matrix gives rise to void growth. The amorphous boundary layer between large spherulites in semicrystalline polymers may also act as starting point for void growth under certain conditions.[5,6] Under high enough dilatational stresses, voids are able to grow in size and coalesce,[7] usually starting at the yield point.[8] Interestingly, void coalescence

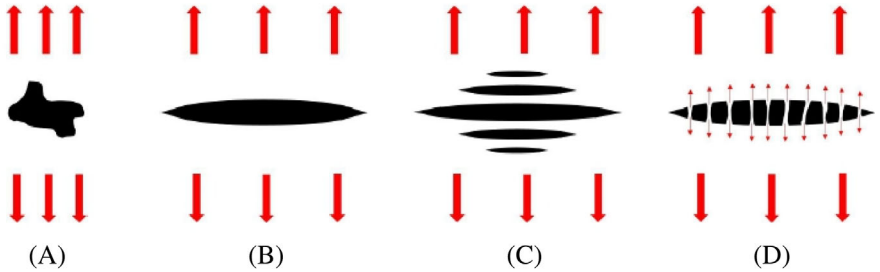

FIGURE 1 Representation of various microdamages and their characteristics, including (A) voids (no aspect ratio and no stress transfer), (B) microcracks (high aspect ratio but no stress transfer), (C) polar fans (column of microcracks), and (D) crazes (high aspect ratio and limited stress transfer)

can lead to larger voids or other classes of damage. While for voids no orientation is assumed, the subsequent mechanisms can be categorized by a characteristic shape and/or aspect ratio. Microcracks, for example, can be seen as an oriented void where two crack flanks join in sharp corners.[9] This gives the defect a high aspect ratio and a slim appearance, which is oriented perpendicular to the main tensile stress. Due to the sharp corners and the lack of stress transfer between the flanks, microcracks have a most detrimental form of notching effect. Thus, cracks grow easily under loading, leading to crack extension and coalescence of microcracks to larger cracks. Over time, the problem enters the domain of fracture mechanics and catastrophic failure may be imminent.[10] Several sources in literature[11–13] report the so-called polar fans specifically in semicrystalline polymers with a well-defined crystal structure. These constructs are localized clusters of microcracks that are aligned parallel to the loading direction. The individual cracks are still separated by thin walls of intact material. Laiarinandrasana et al.[14] found such constructs in polypropylene (PP) as well as polyamide stretching from the poles of spherulites toward the center. The highest density of polar fans was found in the necking area and caused volumetric strains as high as 100%.[15] The final specimen failure happens through coalescence of the individual cracks within one column, followed by catastrophic failure. A craze is a special form of a microcrack and is often described as plane, lens-shaped defect in glassy polymers.[9] It shows mostly the same characteristics as a microcrack, but highly stretched fibrils of polymer are spanned from one edge to the other.[16] Therefore, the craze still has a load bearing capacity to some extent.[17] The fibrils spanning the two crack faces are stretched to their maximum possible elongation. When the craze grows, there are two possibilities for the fibrils to react. When the polymer chains are mobile enough, more material can be drawn in from the surrounding material, so the fibrils become longer and the whole craze wider. This is known as surface drawing or forced reptation.[18] Crazes are able to grow and coalesce through this mechanism.[16] When the material is not mobile enough to perform such a disentanglement process, the fibrils are more likely to fracture. In that case, the craze becomes more similar to a crack the more fibrils are destroyed.[17] While the preferred orientation for crazes is 90° to the major principal stress, Karger-Kocsis and Barany suggest that slight deviations of orientations are possible to avoid running through spherulites or other obstacles, where surface drawing is hindered.[16]

All of these mechanisms are cavitation-inducing processes that involve a dilatational stress component, which is why they never appear under pure compressive stresses. As a consequence, additional volume is created.[13,15,16,19] Voids and crazes do not close on their own and crack healing is unlikely for most materials, especially if the glass transition temperature is significantly above room temperature. Thus, an irreversible change in volume is expected on the microscale. A macroscopic increase in specimen volume is, therefore, a result of microscopic damage.[10] Additionally, the internal load bearing cross section is reduced, which may lead to a strain softening effect.[20] Voids also promote plastic deformation and can in some cases toughen a brittle material by enhancing plasticity.[21,22] Argon and Cohen even suggest that a brittle material response can be avoided by utilizing this characteristic.[23] In conclusion, increases in volume and residual strains, and a decrease of E can be seen as indicators for microstructural damage.[10] Although shear yielding is a common mechanism in polymers too, the formation of shear bands does not directly contribute to the loss of mechanical properties. Instead, the increased plasticity accelerates the nucleation and growth of voids in regions of high hydrostatic stresses.[24,25] Thus, shear yielding is not discussed in detail in this contribution and the focus is set on the resulting voids and cracks. Distinguishing a damage-induced effects from viscoelastic effects is challenging, since their results on a macroscopic level, such as the deterioration of E, may be the same. Therefore, appropriate testing procedures are needed.

To determine the void volume fraction, X-ray tomography scans or scanning electron microscopy (SEM) on cryofractured specimens are an option.[8,19] These methods have to be employed sometime after testing though, so that the majority of relaxation processes is already completed. Comparable in situ measurements are challenging and suffer from various limitations.[8] One major drawback is the limited temporal resolution of many tomography techniques. Therefore, synchrotron radiation is required even for moderate testing speeds.

Olufsen et al. employed a combination of postprocessing techniques and axisymmetric relations for accelerating X-ray tomography to a point where in situ measurements of tensile tests at moderate testing rates are possible and practical.[26] However, this technique also captures creep effects, which may be reversible. In that case, void size is overestimated by the viscoelastic part of the deformation. Additionally, this approach is limited to round bar specimen types to preserve the axisymmetric relations.

Changes to the microstructure affect optical properties as well. Hamza et al. were able to monitor the refractive index during the cold drawing of PP and nylon fibers using a two-beam polarizing interference microscope. On the one hand, changes to the cross-sectional area,[27] the refractive index profile, and the progression of necking[28] could be detected. On the other hand, the evolution of microcracks at high draw ratios was also visible as disturbances in the microinterferograms.[29]

An indirect, qualitative estimation of microstructure is possible by monitoring E or by capturing surface strains using digital image correlation (DIC). Since no visualization of the actual microstructure is given, these techniques should be verified by other methods, such as computed tomography (CT) or SEM.

In this paper, several characterization techniques are compared regarding their suitability to determine irreversible microstructural damage. Simple modifications to well-known standard testing procedures are offered to distinguish between time-dependent and damage-induced decay of material properties of PP. Stress–strain behavior is determined, starting from monotonic tensile tests. Through cyclic load–unload experiments, the decay of E is recorded. Since these experiments are performed under continuous tensile loading, time-dependent creep effects play a significant role. Therefore, a comparison is made to prestrained specimens after relaxation by dynamic mechanical analyses (DMAs), where time-dependent effects are eliminated. Hereby, assumptions are made on the extent of damage as a function of the applied strain, which is verified by CT.

2 | EXPERIMENT

2.1 | Materials

Two different grades of PP were used for the investigations, an ethylene-propylene block-copolymer (PP-B) and a PP homopolymer (PP-H). Basic microscopy under polarized light with a magnification of 50 was sufficient to give a first impression of the crystalline structures of PP-B and PP-H. As shown in Figure 2A, PP-B exhibited a rather undefined crystalline structure and no clear boundaries of spherulites could be seen. This can be explained by the ethylene comonomer units, which hindered the crystallization process of the PP segments.[30] PP-H on the other hand did not suffer from such disturbances in the crystallization phase. Thus, a continuous network of large spherulites could be formed. The average size of spherulites was approximately 50 μm (Figure 2B) and the crystalline structure appeared to be more regular compared to PP-B. The amount of amorphous phase between individual spherulites was assumed to be rather small, since sharp corners could be distinguished between large packages of crystalline phase.

2.2 | Methods

For the tensile testing, dumbbell specimens were prepared from both materials. A crosshead speed of 1 mm/min was used for monotonic tests and cyclic load–unload tests, where increasing amplitudes of applied deformation alternated with unloading steps. Strains and volume changes were recorded using two crossed high-resolution cameras and DIC, so that E could be obtained. It should be mentioned that E, the maximum applied strain, $\varepsilon_{\text{appl}}$, and the residual strain, ε_{res}, were calculated separately for each load–unload loop of the cyclic tensile tests.

A dumbbell specimen shape was chosen for the DMAas well to avoid failure at the clamping. Specimens were prestrained by 0%, 20%, and 40% before being investigated by DMA with a mean stress level of 0.75 MPa and a stress amplitude of 0.5 MPa. The tests were performed at room temperature (23°C) with a frequency of 1 Hz.

Ultimately, high-resolution X-ray CT scans were used to verify the assumptions on damage onset and evolution.

More detailed descriptions on all the methods mentioned above can be found in Appendix A.

2.3 | Characterization of stress–strain behavior

Only the highest strained sections of the specimens were considered for strain evaluation, since material damage often started and progressed in localized regions. These sections were characterized with virtual extensometers in the DIC measurements. Engineering stress and engineering strain, σ_{eng} and ε_{eng}, were calculated using the well-known relations, Equations (1) and (2). Therein, the force, F, was related to the initial cross section A_0 and effects such as necking or volume change due to void formation could not be captured. The true stress, σ_{true}, which takes a certain amount of necking into account, was calculated by Equation (3). This relation was originally designed for metals and assumes that plastic deformation happens under constant volume. While this may

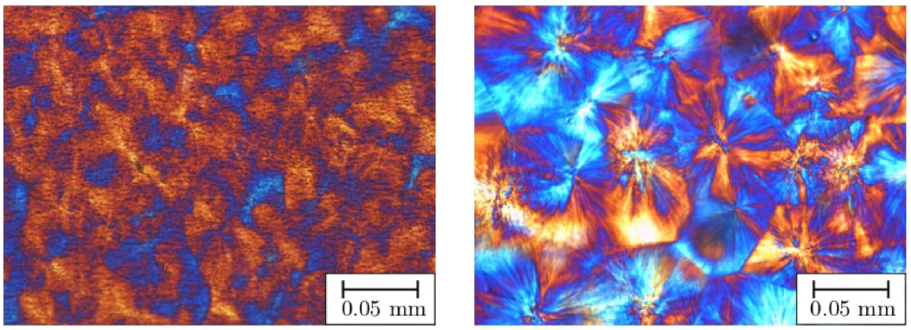

(A) (B)

FIGURE 2 Polarized light micrographs with a magnification of 50 for (A) PP-B and (B) PP-H, both in the undeformed state

be true, for example, for shear yielding,[9,17] errors could arise for materials that are prone to void formation or crazing. In these cases, the lateral contraction may be overestimated, since the creation of additional volume inside the material has not been considered. This results in a calculated cross-sectional area that is too small and risks overestimating the stresses. In this contribution, the DIC measurements were used to directly measure the real width and thickness, b_{real} and h_{real}, that occurred at the narrowest specimen section. Using the real cross section, A_{real}, the real stress, σ_{real}, could be calculated (Equations 4 and 5). While this consideration did not consider the loss of internal cross section due to voids, it was still the most accurate estimate that could be made at a macroscopic level. Even more accurate measurements of volume would only be possible by using spectroscopic methods such as in situ tomography. For the sake of simplicity and comparability, all stresses were correlated to the corresponding values of ε_{eng}. In all monotonic tests, E was evaluated according to ISO 527.

$$\sigma_{\text{eng}} = \frac{F}{A_0} \tag{1}$$

$$\varepsilon_{\text{eng}} = \frac{\Delta l}{l_0} \tag{2}$$

$$\sigma_{\text{true}} = \sigma_{\text{eng}}\left(1+\varepsilon_{\text{eng}}\right) \tag{3}$$

$$A_{\text{real}} = b_{\text{real}} h_{\text{real}} \tag{4}$$

$$\sigma_{\text{real}} = \frac{F}{A_{\text{real}}} \tag{5}$$

2.4 | Volume change as sign of damage onset

As mentioned in the introduction and stated by literature, many damage mechanisms are accompanied by an increase in volume.[13,15,16,19] To capture such effects, a normalized volume element, V_{norm}, was calculated from the engineering strains in all three spatial directions (Equation 6 and Figure 3A). These strains were captured in DIC measurements using virtual extensometers (Figure A2B), whereas the load was applied in the y-direction in all experiments. During the monotonic tests, V_{norm} was monitored and served as first indicator of damage onset. However, other effects, such as viscoelastic creep, may also have contributed to the increased volume.

$$\begin{aligned} V_{\text{norm}} &= \frac{V_{\text{real}}}{V_0} = \frac{b_{\text{real}} h_{\text{real}} l_{\text{real}}}{b_0 h_0 l_0} \\ &= \left(1+\varepsilon_{\text{eng},x}\right)\left(1+\varepsilon_{\text{eng},y}\right)\left(1+\varepsilon_{\text{eng},z}\right) \end{aligned} \tag{6}$$

When plotted against the applied strain, V_{norm} started to increase at a higher rate upon reaching the yield point. This transition point was approximated with two linear regression lines, as shown in Figure 3B, to determine the strain at the intersection point, ε_{vol}. This parameter describes the starting point of accelerated volume increase and may serve as indicator for the onset of material damage with volume change. For stress–strain curves that have a very fluent yield region without a maximum in stress, ε_{vol} could even be used to determine a yield point, if no other options are available.

3 | RESULTS AND DISCUSSION

3.1 | Differences between stress–strain evaluation methods

As a starting point for the investigation, the monotonic tensile tests are chosen. For polymers, the yield point in such experiments is generally determined as the first local maximum in the stress–strain curve, which is often the onset for the necking process. However, time-dependent effects as well as damage to the microstructure cannot be deduced during the experiment, unless the damage is so extensive that it becomes visible, for

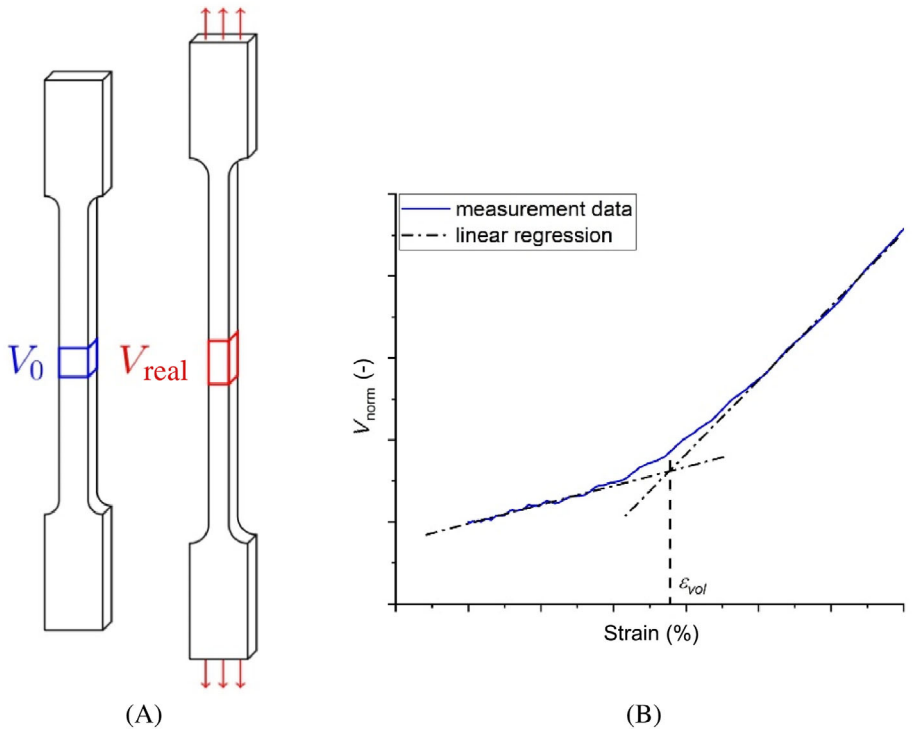

FIGURE 3 (A) Volume change due to specimen deformation and (B) determination of ε_{vol}

example, as stress whitening or tearing. To gain additional information, V_{norm} was also monitored. Figure 4A, B depicts representative stress–strain curves and the variations of V_{norm} for PP-B and PP-H, whereas the numeric results are listed in Table 1. At first glance, the two materials show a similar stress–strain behavior. Especially the evaluation of E appears unaffected by the method of evaluation (engineering stress–strain, true stress–strain, real stress–strain), although some small differences can be noted in other parts of the curves. PP-H shows approximately 20% higher values of E and σ_{UTS} in comparison with PP-B. The strain at break is high in both cases, but a high data scattering occurred too. When judging only by engineering stress–strain curves, PP-B and PP-H only show strain softening behavior after the yield point. However, this is an error due to extensive necking effects, which are not uncommon for PP. When considering true or real stress–strain curves, both materials show strain hardening after the yield point, presumably caused by cold drawing of the macromolecules. At very high strains, a reduction in stress can be observed as a consequence of extensive material damage. At this advanced stage of damage, the specimens start to slowly tear apart before failing completely. This decrease in stress starts earlier for PP-B than for PP-H. To sum up, engineering stress–strain curves are good approximations for small strains, but for higher deformations other approaches should be considered. As expected, the true stress values overestimate the stresses but give an overall good impression of material behavior. For both materials, the true stress–strain method seems to underestimate the cross-sectional area, because the changes in volume due to damaging mechanisms are not accounted for. As a result, true stresses at high strains tend to be higher than the real stresses by approximately 15% for PP-B and 20% for PP-H. The real stress–strain method is the most precise due to measuring the actual dimensions of the specimens. Therefore, this method will be used in all further considerations.

The development of V_{norm} over the course of the experiment is also shown in Figure 4. Until to the yield point, V_{norm} remains low for both materials before starting to rise steadily. The point of increased volume gain at ε_{vol} coincides well with the strain at yield point, ε_y, for both PP-B and PP-H. For PP-B, the beginning of specimen failure is accompanied by an increased rate of volume gain, which is not seen in PP-H. In general, PP-B exhibits a higher increase of V_{norm} than PP-H, indicating that the block-copolymer is more susceptible to the formation of voids, cracks, or crazes. Kim et al.[31] suggest, for example, that domains of a second phase or fillers within a matrix play a major role in void formation. Namely, the foreign phases provide initial stress concentrations, which enable the cavitational processes in the first place. Other sources, for example, Kawai et al.[32] claim that the amorphous regions within the material serve as origin of void formation. This may also be a plausible explanation for the increased volume gain of PP-B, which appears to have a less organized crystal structure than PP-H (see Figure 2A vs. Figure 2B). At the end of the experiments, V_{norm} starts dropping for both materials

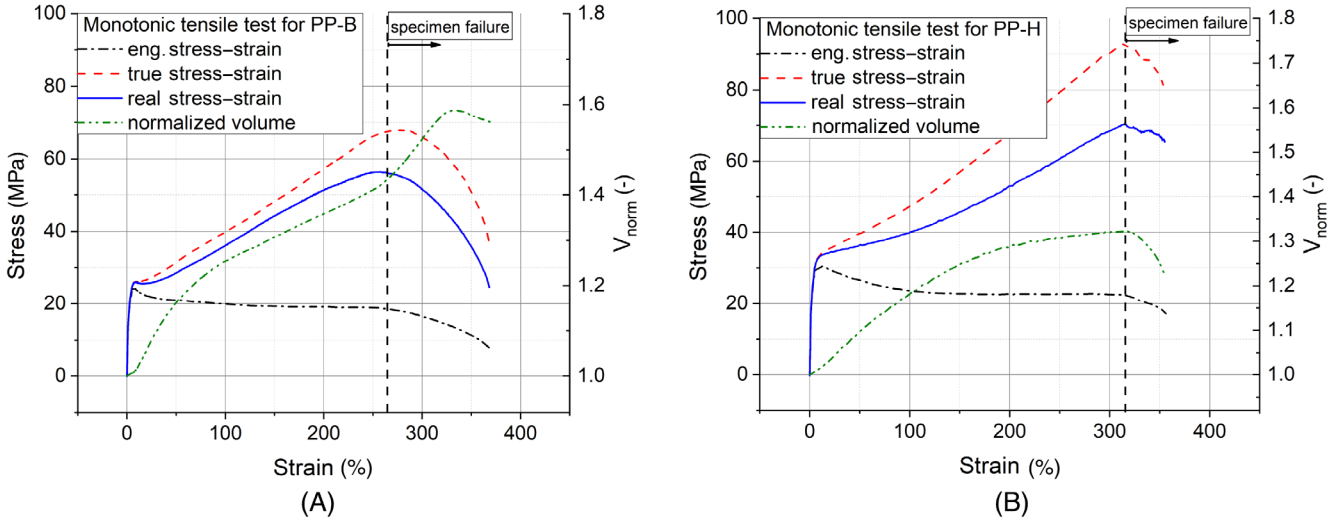

FIGURE 4 Stress–strain curves and normalized volume for (A) PP-B and (B) PP-H, whereas the differences between engineering stress–strain, true stress–strain, and real stress–strain evaluations are visible

TABLE 1 Material parameters obtained from monotonic tensile tests

	PP-B			PP-H		
	Eng.	**True**	**Real**	**Eng.**	**True**	**Real**
E (MPa)	1435 ± 44	1450 ± 52	1444 ± 52	1773 ± 56	1801 ± 69	1800 ± 69
σ_y (MPa)	23.9 ± 0.4	26.0 ± 0.3	25.8 ± 0.2	30.8 ± 0.3	33.8 ± 0.3[a]	33.3 ± 0.4[a]
σ_{UTS} (MPa)	23.9 ± 0.4	64.8 ± 14.1	55.7 ± 12.5	30.8 ± 0.3	108.7 ± 39.8	86.7 ± 37.6
ε_y (%)	9.7 ± 0.4			11.0 ± 3.3		
ε_{vol} (%)	9.5 ± 0.6			9.5 ± 0.5		
ε_{fr} (%)	291 ± 90			428 ± 151		

[a]In some cases, where no distinguished maximum appears in the real stress–strain curves, the stresses at ε_y of the engineering stress–strain curve are taken as σ_y.

as a result of the decreased stresses. However, both materials show noticeable increases of their volume (up to 60% for PP-B and 30% for PP-H), which is a strong indicator for damage in conjunction with volume gain. Thus, a decay of material properties is expected as the applied strain increases.

3.2 | Property deterioration including time-dependent effects

Cyclic load–unload experiments were used to illustrate the deterioration of material properties under tension, which was not possible during the monotonic tests. For each cycle, the values for E and ε_{res} as a function of ε_{appl} of one representative specimen per material are shown in Figure 5A. Figure 5B shows the first 45% of strain in greater detail. Therein it is worth noting that the data points for PP-B and PP-H are not equally spaced. This is due to differences in the localization of strain between the two materials. PP-B shows moderate strains in the midsection of the specimens throughout the whole experiment. PP-H on the other hand exhibits a very uniform distribution of strain over the whole specimen for the low initial deformations, leading to a dense population of measurement points at the start of the curve. However, the necking process happens very localized, leading to large steps in local strain for higher displacements. Interestingly, ε_{res} as a function of ε_{appl} is nearly identical for PP-H and PP-B. The results suggest increased plastic deformation after 5% of applied strain, since ε_{res} starts rising at higher rates. This is only half of the strain one would expect from the monotonic experiments, where yielding started around 10%. Even at low strains, no reversible regime can be observed, as ε_{res} is always >0. For larger strains, ε_{res} increases linearly with a slope close to 1, which means that ε_{res} increases almost as fast as ε_{appl}. This is an indicator of highly plastic behavior,

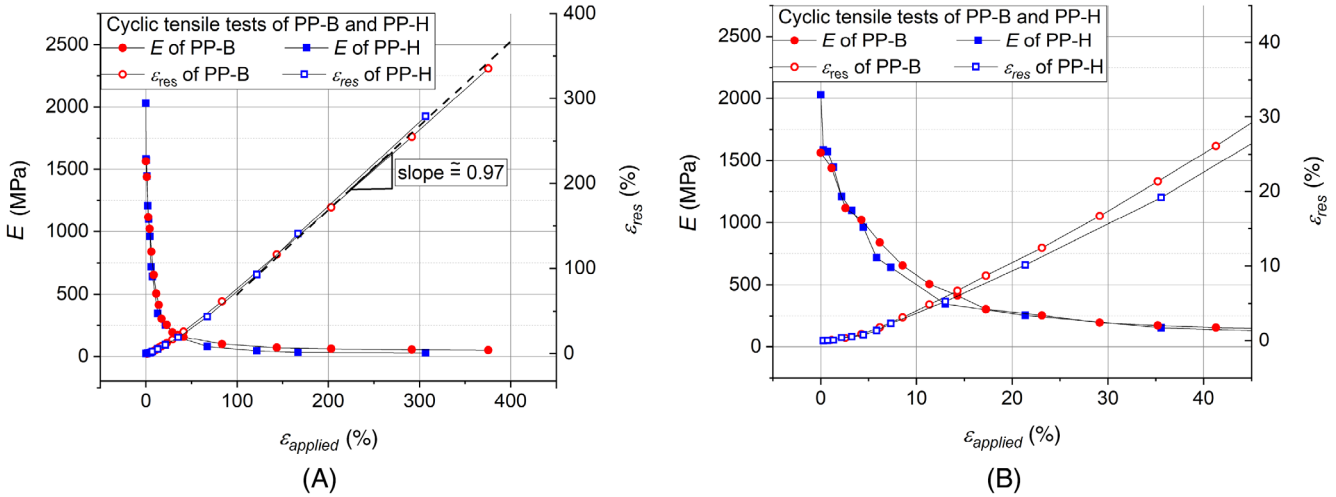

FIGURE 5 Development of modulus and residual strain as a function of the applied strain, evaluated for each cycle in load–unload experiments. Values are depicted (A) throughout the whole experiment and also (B) for the first 45% of strain only

although one cannot distinguish between irreversible plastic behavior and slow components of viscoelastic deformation. Ognedal et al. reported similar findings, stating that the elastic retraction of the material is reduced, the higher the applied strains become.[8] The decay of modulus is striking in both materials, with E dropping to mere fractions of its initial value within 5%–10% of ε_{appl}. The only noticeable difference is that PP-H starts at higher values than PP-B. This is surprising, considering that the microstructures of the homopolymer and the block-copolymer are supposedly different and distinct differences were found in the monotonic tests. Furthermore, the increased stiffness and strength of PP-H should have at least some influence on material properties at higher strains. The testing temperature is above the glass transition temperature for both materials. Thus, it is reasonable to assume that the amorphous PP regions will be the main contributors to long-term deformation, since all crystalline structures are still in their solid state. The materials may therefore also behave similarly under long-term loading, because PP-H and PP-B are both based on a comparable PP backbone. The authors propose that this viscoelastic creep is the dominant factor for the two investigated materials in load–unload experiments. Therefore, initial differences in properties become irrelevant as time progresses. To reach a conclusion on the time-independent effects of loading, two additional questions need to be answered:

1. What are the differences in material behavior when viscoelastic effects are avoided by giving the materials time to relax?
2. What are the differences in microstructure between PP-H and PP-B in the damaged and undamaged state?

3.3 | Property deterioration excluding time-dependent effects

A number of adaptations to the testing procedure have to be made to exclude viscoelastic effects while determining E. On the one hand, high tensile stresses for prolonged periods of time have to be avoided at all costs. On the other hand, sample size and shape play an important role for subsequent imaging techniques. DMA of prestrained specimens is the method of choice in this contribution. Applied forces and displacements are very small compared to tensile testing, while the instrumentation is precise enough to reliably determine E. As another indication of damage, the mechanical loss factor tan δ can also be obtained in DMA measurements. Additionally, the specimen size is small enough, so that micro-CT measurements can be employed to analyze the microstructure, even without the need to further dissect the specimens. Since the material is given 7 days to relax, all time-dependent processes are assumed to be completed. The values of E and tan δ as a function of ε_{appl} are shown in Figure 6 for PP-H and PP-B. In both cases, the starting modulus tends to be slightly higher than for the tensile tests, which could be caused by the increased loading rate in the DMA procedure. Additionally, E is evaluated at smaller strains in a DMA experiment than in a tensile test, which is also likely to cause increased values. Most interestingly, E of both materials remains high for much higher levels of strain compared to the cyclic tensile tests. More specifically, a noticeable decrease in E for PP-B cannot be seen until 10% of prestrain and PP-H even shows an increase in modulus after 15% of prestrain. In comparison with the load–unload experiments, the prestrained DMA method shows the differences in material behavior much more clearly, since time-dependent effects no longer distort

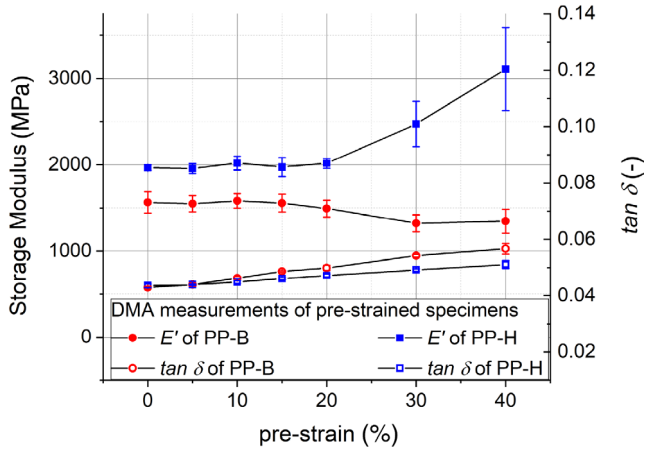

FIGURE 6 Storage modulus and mechanical loss factor versus prestrain for PP-H and PP-B, measured in dynamic mechanical analysis (DMA) experiments of prestrained specimens at room temperature (23°C) with a frequency of 1 Hz

the results. A harsh decrease in stiffness cannot be seen at all, which indicates that the previously observed modulus decay (see Figure 5) is primarily caused by creep effects. The loss factor tan δ shows a slow and steady increase in both materials, suggesting at least some detrimental changes of the microstructures in both materials. To validate these assumptions, the microstructures of the two PP types are investigated using micro-CT.

3.4 | Analysis of microstructure

While a first impression of microstructure could be obtained in polarized light microscopy, some defects may be too small for the resolution of polarized light microscopy. Some defects might also have been destroyed during the preparation of the thin slices. In addition to that, a three-dimensional representation of the microstructure

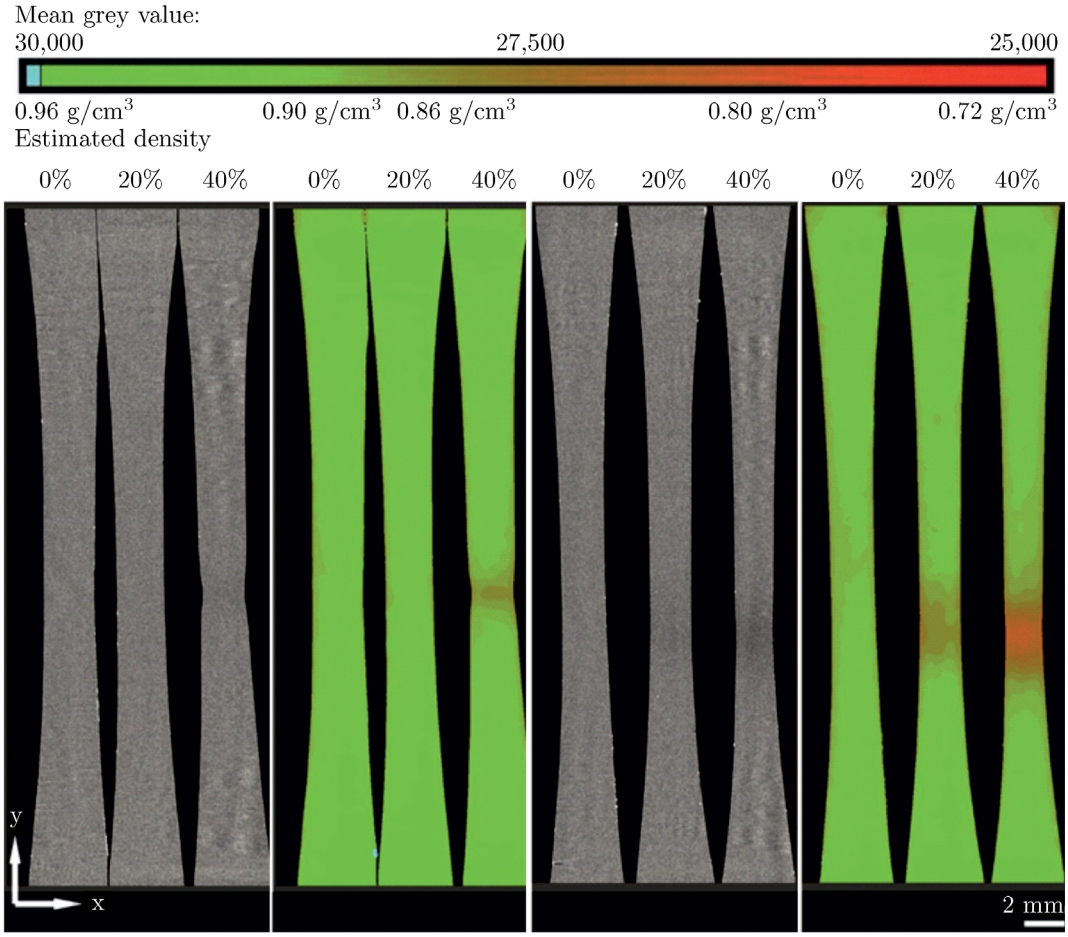

FIGURE 7 Frontal (y–x) slice images from computed tomography (CT) measurements showing (A) PP-H, (B) PP-H estimated density, (C) PP-B, and (D) PP-B estimated density at 0%, 20%, and 40% prestrain scanned at (16.5 μm)^3 voxel size. (A) and (C) Gray values corresponding to absorption contrast and (B) and (D) red and green visualizations of these gray values and estimated material densities

TABLE 2 Density and porosity estimated from CT gray values

	PP-B			PP-H			
	0%	**20%**	**40%**	**0%**	**20%**	**40%**	**Air**
Gray value	28,783	27,973	26,684	28,788	28,770	28,043	10,008
ρ (g/cm^3)	0.90[a]	0.86	0.80	0.90[a]	0.90	0.86	0.0
Porosity (vol%)	0.0	4.31	11.18	0.0	0.10	3.97	0.0
E (MPa)[b]	1565 ± 124	1493 ± 99	1345 ± 140	1965 ± 32	2017 ± 57	3110 ± 480	0.0

Abbreviations: CT, computed tomography; DMA, dynamic mechanical analysis.
[a]Values from material datasheet.
[b]Values from DMA measurements.

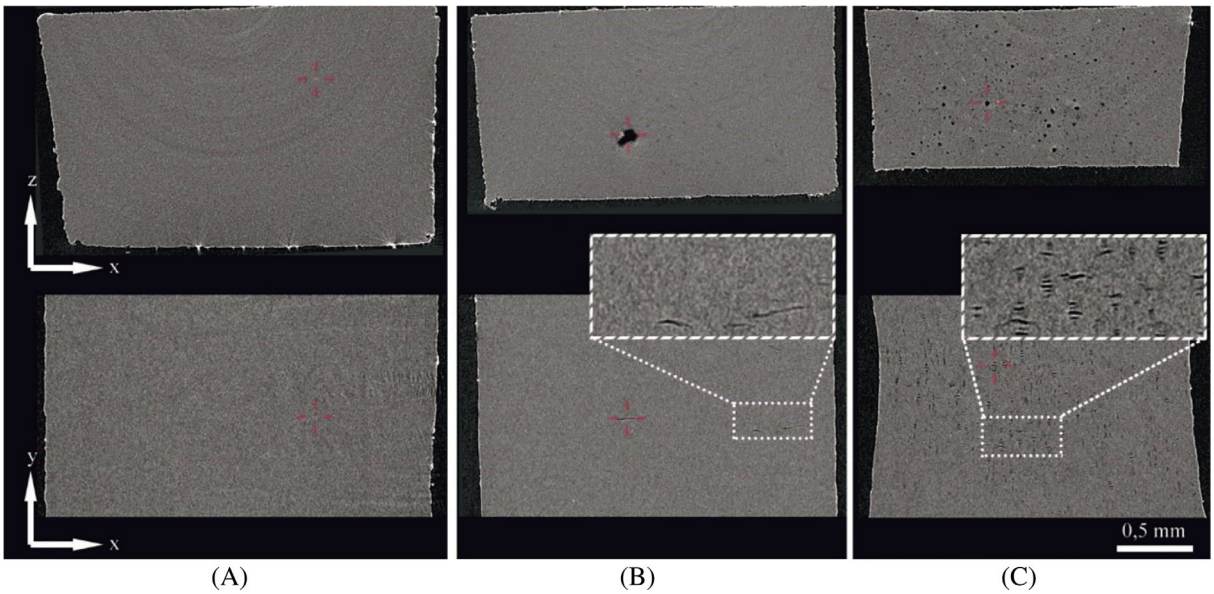

FIGURE 8 Axial (z–x) and frontal (y–x) slice images from computed tomography (CT) measurements showing PP-H at (A) 0% (E = 1965 ± 32 MPa), (B) 20% (E = 2017 ± 57 MPa), and (C) 40% (E = 3110 ± 480 MPa) prestrain scanned at (1.25 μm)^3 voxel size

cannot be easily obtained from transmitted light microscopy. Therefore, CT measurements are used to investigate the microstructure more closely at 0%, 20%, and 40% applied strain. In the overview scan in Figure 7 performed at (16.5 μm)^3 voxel size, no structural information of damages such as micro cracks or crazes can be seen in any of the investigates samples. Thus, they are expected to be far below the chosen voxel size. But as also shown in the literature,[33] nonvisible defects can lead to a reduction of gray values in the CT images, representing the absorption contrast of X-rays. Therefore, the presence of defects leads to a reduction of X-ray absorption, which is visible in Figure 7A for PP-H 20% and 40% as well in Figure 7C for PP-B 20% and 40%. For better visualization of these small changes in gray values, in Figure 7B,D, the gray values were set to green and red color tones. In addition, a local density in each position of the sample can be estimated by applying the rules of mixture. Table 2 lists the minimal average gray values in the cross section of the different specimens and estimated density and porosity, respectively.

Based on the overview CT scans, the regions for the high-resolution scans were defined in the regions with the highest estimated porosity values and scans at (1.25 μm)^3 voxel size are performed (depicted in Figures 8 and 9). In the reference state samples (0% prestrain), no signs of damage can be seen. However, smaller inhomogeneities of higher density, presumably caused during processing, can be distinguished. For the specimens at 20% prestrain, first signs of damage are clearly visible. While the number and size of defects is relatively low for PP-H (Figure 8), PP-B already shows numerous defects present in the microstructure (Figure 9). As a result, the modulus for PP-H remains at its initial value up to this point, while PP-B already displays a decreased E (modulus values taken from prestrained DMA measurements). One explanation for the

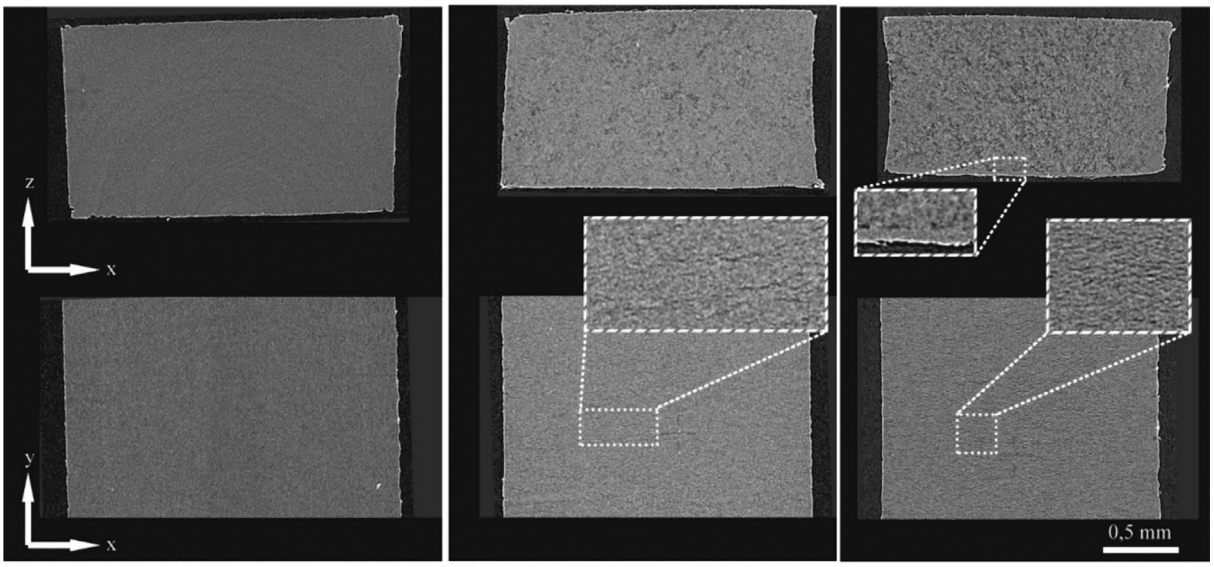

FIGURE 9 Axial (z–x) and frontal (y–x) slice images from computed tomography (CT) measurements showing PP-B at (A) 0% ($E = 1565 \pm 124$ MPa), (B) 20% ($E = 1493 \pm 99$ MPa), and (C) 40% ($E = 1345 \pm 140$ MPa) prestrain scanned at $(1.25\ \mu m)^3$ voxel size

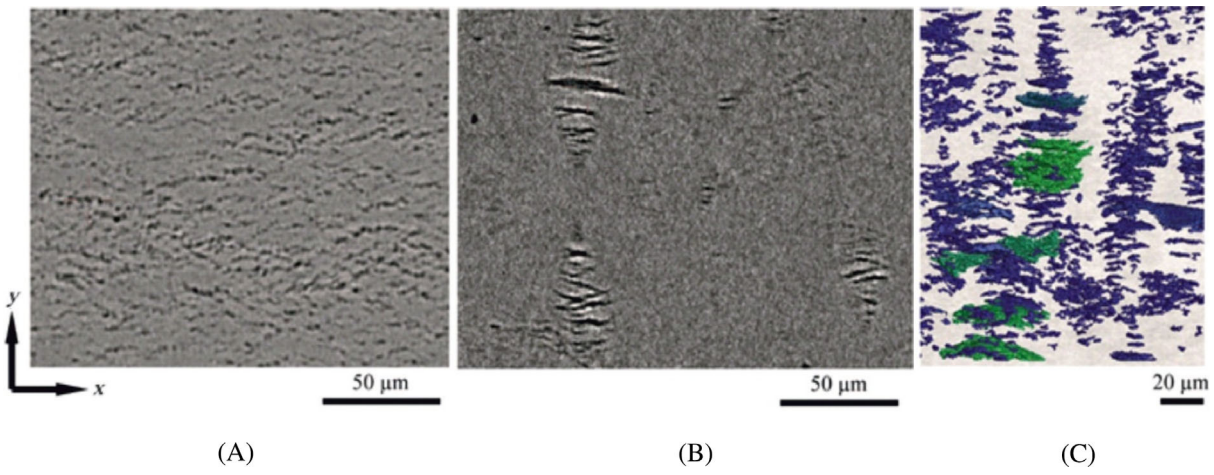

FIGURE 10 Frontal (y–x) slice images from computed tomography (CT) measurements showing (A) PP-B and (B) PP-H at 40% prestrain scanned at $(0.5\ \mu m)^3$ voxel size. (C) Three-dimensional (PP-B at 40%) rendering of segmented defect structures is shown by applying a manual threshold

increased resilience of PP-H against crazing could be its well-defined crystal structure. The reduced amount of amorphous and heterogeneous phases may hinder the formation of voids under strain,[31,32] so that the subsequent progress of damage mechanisms could be impeded as well. Since the number of microcracks increases the more strain is applied, the modulus of PP-B further decreases up to 40% prestrain (see Figure 6). For PP-B, the loss of load bearing cross section is comparably large due to the microcracks being spread randomly throughout the material. Interestingly, PP-H shows an increase in E between 20% and 40% prestrain despite the starting accumulation of damage (as shown in Figure 8). Although a number of defects can be seen, the mechanical properties are not yet compromised by the loss of load bearing cross section. Fortunately, the damage in PP-H appears very localized, so only small areas of cross section are affected at a time. Instead, it appears that that the load bearing capacity of the macromolecules is maximized due to an increased degree of orientation (similar to a cold drawing effect). The assumption of increased orientations is also supported by Figure 4, where strain hardening can be seen on a macroscopic level. However, the modulus is expected to decrease again for strains exceeding 40%, when extensive

microstructural damage begins to outweigh the orientation effect.

Figure 10 shows the results from the CT scans performed at highest possible resolution for this sample size, reaching a voxel size of $(0.5\ \mu m)^3$. Compared to Figure 9 now also for the PP-B 40% specimen (Figure 10A), very clear microcrack structures can be resolved and become visible. Crack widths for PP-B are all in the range of a few voxels and even below. In Figure 10B, localized polar fans can be distinguished clearly for the PP-H 40% sample, but nearly no smaller microcracks appear in the remaining polymer. As mentioned in the introduction, such structures have been reported before in semicrystalline polymers with well-defined spherulites.[13–15] On the other hand, crazes can be ruled out as damaging mechanism, since no fibrils stretching across the crack flanks are visible. A segmentation by a manually defined threshold results in a defect content of ~10 vol% for PP-B at 40% strain and 2 vol% for PP-H at 40% strain. These values are in the order of magnitude of the estimated porosity from Table 2. In Figure 10C, such a segmentation is visualized as three-dimensional rendering of a small region from the PP-H 40% specimen. It is worth noting that these porosity values are recorded in the relaxed and unloaded state of the specimen, so that a comparison to the volume increase in the monotonic tensile tests (Figure 4) is not advisable. All of the trends discovered in the CT measurements are in good agreement with the previously conducted prestrained DMA experiments. Thus, the prestrained DMA may serve as complementary method for CT measurements. It could be used as convenient, low-cost tool for the preselection of the most relevant specimens, before conducting high-resolution CT as a more thorough investigation. The CT measurements also confirm the prestrained DMA as the most reliable of the methods discussed to estimate damage, without creep interactions in a material.

4 | CONCLUSION

Different measurement techniques are investigated to capture the damage-induced and time-dependent deterioration in mechanical properties of the semicrystalline polymer PP. Two different grades are tested, namely an ethylene-propylene block-copolymer and a PP homopolymer.

In monotonic tensile tests, the true stress–strain behavior, which includes necking as well as three-dimensional volume change during testing, is captured using DIC of two crossed cameras. The elastic modulus, E, is only available at the start of the measurement, making the change in volume the only parameter to monitor the state of the material. This volume is found to increase the more strain is applied, especially after the yield point has been reached.

In cyclic load–unload experiments, the decrease of E with each cycle of increased loading can be studied over a wide range of applied strains. E starts plummeting in the same fashion for both investigated polymers after small amounts of strain are applied. Simultaneously, the residual strain after each cycle is found to drastically increase over the course of the experiment. It is shown that the decrease in E is mainly caused by viscoelastic effects due to the extended duration of tensile loading, making this method ill-suited to characterize damage to the microstructure. However, the values of E under the combined influence of damage and viscoelasticity can be monitored throughout the whole experiment.

In contrast to that, prestrained specimens are analyzed using DMA. Due to a relaxation period between the prestraining and the DMA measurements, time-dependent effects are eliminated. E retains higher values in these experiments until a certain amount applied strain (10%–15% in the investigated materials). Afterward, the modulus starts either to decrease as a result of damage or increase as a result of increased molecule orientation. All in all, this method yields a better representation of the integrity of the investigated materials by excluding viscoelastic effects.

Finally, the damages to microstructure are illustrated in high-resolution computer tomography of specimens that were strained by 0%, 20%, and 40%. Therein, the investigated PP block-copolymer is prone to extensive microcracking throughout the whole specimen. The PP homopolymer on the other hand shows localized damage in the form of polar fans, which are clusters of microcracks, along the polar axis of spherulites. The increasing amount of internal damage is made visible and is found to be in good agreement with the prestrained DMA measurements. Therefore, prestrained DMA experiments may be considered as a tool to preselect specimens. Subsequent CT investigations would then only need to be performed on specimens of the most interest, thus saving time and effort.

ACKNOWLEDGMENTS

This research was supported by the Austrian Research Promotion Agency (FFG) as part of the project "Entwicklung und Optimierung von hoch risszähen, polymeren Mehrschicht-Verbundsystemen nach biomimetischen Prinzipien," grant agreement 858562, referred to with the acronym "BioMimicPolymers." CT scans and evaluations were performed within the projects "BeyondInspection (grant number: 874540)" and "pore3D (grant number: 868735)." Both CT projects were funded by the State Government of Upper Austria and Austrian Research Promotion Agency (FFG).

DATA AVAILABILITY STATEMENT

The data that support the findings of this study are available from the corresponding author upon reasonable request.

ORCID

Johannes Wiener https://orcid.org/0000-0002-0956-7420
Florian Arbeiter https://orcid.org/0000-0003-4638-0849

REFERENCES

[1] A. Galeski, *Prog. Polym. Sci.* **2003**, *28*(12), 1643.
[2] V. Delhaye, A. H. Clausen, F. Moussy, R. Othman, O. S. Hopperstad, *Int. J. Impact Eng.* **2011**, *38*(4), 208.
[3] V. Delhaye, A. H. Clausen, F. Moussy, O. S. Hopperstad, R. Othman, *Polym. Test.* **2010**, *29*(7), 793.
[4] H. S. Katz, J. V. Milewski, *Handbook of Fillers for Plastics*, Van Nostr and Reinhold, New York **1987**. ISBN: 978-0-442-26024-8.
[5] J. L. Way, J. R. Atkinson, J. Nutting, *J. Mater. Sci.* **1974**, *9*(2), 293.
[6] J. M. Schultz, *Polym. Eng. Sci.* **1984**, *24*(10), 770.
[7] T. F. Guo, J. Faleskog, C. F. Shih, *J. Mech. Phys. Solids* **2008**, *56*(6), 2188.
[8] A. S. Ognedal, A. H. Clausen, T. Berstad, T. Seelig, O. S. Hopperstad, *Int. J. Solids Struct.* **2014**, *51*(7–8), 1494.
[9] W. Retting, *Mechanik der Kunststoffe: Die mechanischen Eigenschaften von Polymer-Werkstoffen*, Hanser, Munich **1992**. ISBN: 3446161015.
[10] A. S. Ognedal, A. H. Clausen, A. Dahlen, O. S. Hopperstad, *Mech. Mater.* **2014**, *72*, 94.
[11] G. Boisot, L. Laiarinandrasana, J. Besson, C. Fond, G. Hochstetter, *Int. J. Solids Struct.* **2011**, *48*(19), 2642.
[12] A. Pawlak, A. Galeski, *Macromolecules* **2008**, *41*(8), 2839.
[13] H.-A. Cayzac, K. Sai, L. Laiarinandrasana, *Int. J. Plast.* **2013**, *51*, 47.
[14] L. Laiarinandrasana, N. Selles, O. Klinkova, T. F. Morgeneyer, H. Proudhon, L. Helfen, *Polym. Test.* **2016**, *55*, 297.
[15] L. Laiarinandrasana, T. F. Morgeneyer, H. Proudhon, F. N'guyen, E. Maire, *Macromolecules* **2012**, *45*(11), 4658.
[16] J. Karger-Kocsis, T. Barany, *Polypropylene Handbook*, Springer International Publishing, Cham **2019**. https://doi.org/10.1007/978-3-030-12903-3
[17] W. Grellmann, B. Langer, *Deformation and Fracture Behaviour of Polymer Materials*, Springer International Publishing, Cham **2017**. https://doi.org/10.1007/978-3-319-41879-7
[18] T. C. B. McLeish, C. J. G. Plummer, A. M. Donald, *Polymer* **1989**, *30*(9), 1651.
[19] S. N. Olufsen, K. R. Tekseth, D. W. Breiby, A. H. Clausen, O. S. Hopperstad, *Polym. Test.* **2020**, *91*, 106834. https://doi.org/10.1016/j.polymertesting.2020.106834
[20] J. Mohanraj, D. C. Barton, I. M. Ward, A. Dahoun, J. M. Hiver, C. G'Sell, *Polymer* **2006**, *47*(16), 5852.
[21] Z. Bartczak, A. S. Argon, R. E. Cohen, M. Weinberg, *Polymer* **1999**, *40*(9), 2347.
[22] I. Kemal, A. Whittle, R. Burford, T. Vodenitcharova, M. Hoffman, *Polymer* **2009**, *50*(16), 4066.
[23] A. S. Argon, R. E. Cohen, *Polymer* **2003**, *44*(19), 6013.
[24] A. L. Gurson, *J. Eng. Mater. Technol.* **1977**, *99*(1), 2.
[25] V. Tvergaard, A. Needleman, *Acta Metall.* **1984**, *32*(1), 157.
[26] S. N. Olufsen, A. H. Clausen, D. W. Breiby, O. S. Hopperstad, *Mech. Mater.* **2020**, *142*, 103296. https://doi.org/10.1016/j.mechmat.2019.103296
[27] A. A. Hamza, T. Z. N. Sokkar, M. A. El-Bakary, *Meas. Sci. Technol.* **2004**, *15*, 831.
[28] A. A. Hamza, T. Z. N. Sokkar, M. A. El-Bakary, A. M. Ali, *Opt. Laser Technol.* **2010**, *42*, 703.
[29] A. A. Hamza, A. E. Belal, T. Z. N. Sokkar, M. A. El-Bakary, K. M. Yassien, *J. Opt. A: Pure Appl. Opt* **2007**, *9*, 820.
[30] Z. Bartczak, A. Galeski, E. Martuscelli, *Polym. Eng. Sci.* **1984**, *24*(15), 1155.
[31] G. M. Kim, G. H. Michler, M. Gahleitner, J. Fiebig, *J. Appl. Polym. Sci.* **1996**, *60*(9), 1391.
[32] T. Kawai, S. Soeno, S. Kuroda, S. Koido, T. Nemoto, M. Tamada, *Polymer* **2019**, *178*, 121523.
[33] J. Kastner, C. Gusenbauer, S. Senck & G. Rao in: Proceedings of 15th Asia Pac. Conf. Non-Destr. Test. (APCNDT 2017), Singapore, November 2017, pp. 7. https://www.ndt.net/search/docs.php3?id=22081
[34] B. Plank, M. Schiwarth, S. Senck, J. Herr, S. Ayalur-Karunakaran & J. Kastner in: Proceedings of Int. Symp. Digit. Ind. Radiol. Comput. Tomogr. (DIR 2019), Germany, July 2019, pp. 11. https://www.ndt.net/search/docs.php3?id=24749
[35] L. A. Feldkamp, L. C. Davis, J. W. Kress, *J. Opt. Soc. Am. A* **1984**, *1*(6), 612. https://doi.org/10.1364/JOSAA.1.000612.
[36] A. Khudiakova, M. Berer, S. Niedermair, B. Plank, E. Truszkiewicz, G. Meier, H. Stepanovsky, M. Wolfahrt, G. Pinter, J. Lackner, *Addit. Manuf.* **2020**, *36*, 101671. https://doi.org/10.1016/j.addma.2020.101671
[37] J. Kastner, B. Plank, D. Salaberger & J. Sekelja in: Proceedings of 2nd Int. Symp. NDT Aerosp., November 2010, pp. 12. https://www.ndt.net/search/docs.php3?id=10410
[38] P. S. Stelzer, B. Plank, Z. Major, *Nondestruct. Test. Eval.* **2020**, *35*(3), 342.
[39] P. Weissenbacher MSc Thesis, University of Applied Sciences Upper Austria, 2019.
[40] A. Y. Raja, M. Moghiseh, C. J. Bateman, N. De Ruiter, B. Schon, N. Schleich, T. B. F. Woodfield, A. P. H. Butler, N. G. Anderson, *Appl. Sci.* **2018**, *8*, 467.

How to cite this article: J. Wiener, F. Preissegger, B. Plank, F. Arbeiter, O. Kolednik, G. Pinter, *Polym. Eng. Sci.* **2022**, *62*(6), 1959. https://doi.org/10.1002/pen.25979

APPENDIX A

A.1 | EXPERIMENTAL DETAILS

A.1.1. | Specimen preparation

Dumbbell specimens for monotonic and cyclic tensile tests were machined from 4-mm-thick extruded sheets of PP-H and PP-B. In all cases, the length axis of the specimens was parallel to the direction of extrusion. The exact dimensions are shown in Figure A1. To accommodate the small dimension of the dynamic mechanical analysis (DMA) apparatus,

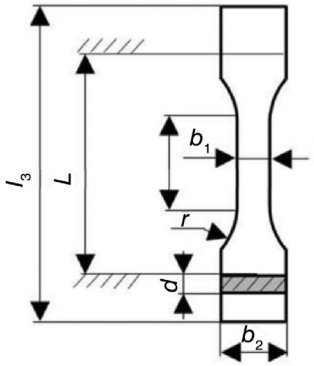

	Specimen feature	Tensile specimens	DMA specimens
l_3	Total length (mm)	80	50
l_1	Parallel length (mm)	15	10
L_1	Clamping length (mm)	42	35
b_1	Minimum width (mm)	10	2.3
b_2	Shoulder width (mm)	23	4
d	Thickness (mm)	4	1.3

FIGURE A1 Specimen dimensions for tensile tests and dynamic mechanical analysis (DMA)

miniature specimens had to be sanded from thin slices of the same 4-mm-thick plates. The dimensions are also given in Figure A1. The dumbbell form was used instead of prismatic specimens to ensure that damage would occur localized in the center of the specimen. This was necessary, since preliminary tests showed a tendency of the material to yield and fail at the clamping. This has to be kept in mind, when comparing exact modulus values, as the introduction of force and the resulting stress state in prismatic specimens are different from dumbbell specimens.

A.1.2. | Test setup for tensile tests

Monotonic and cyclic tensile tests were performed on a Zwick Z010 (Zwick/Roell, Ulm, Germany) at a crosshead speed of 1 mm/min and ambient conditions. In the monotonic tests, specimens were continuously loaded until fracture. A total of four specimens was tested per material. For the cyclic tests, a load–unload procedure was employed. The specimens were deformed with a rate of 1 mm/min until a predetermined displacement was reached. Then, the specimen was unloaded using a crosshead speed of 1 mm/min. After unloading to zero force, the next loading step was started immediately without time for relaxation. By increasing the maximum displacement from step to step, the specimens were tested until fracture. The increments of displacement were 0.5 mm for displacements between 0 and 5 mm, 1 mm between 5 and 10 mm, 5 mm between 10 and 25 mm, and 15 mm until fracture. Due to the extensive testing time of this procedure, only three specimens were tested per material. The deformations of the test specimens were monitored using cameras in a 90° angle as shown in Figure A2A so that a front view as well as a side view of the specimen could be obtained. Two Prosilica GT6600 (Allied Vision Technologies GmbH, Stadtroda, Germany) equipped with 100-mm Tokina AT-X M100 PRO D macro objectives (Kenko Tokina Co., Nakano, Japan) were used for that purpose. Digital image correlation of the surface strains was performed using the software package Mercury 2.8 (Sobriety s.r.o., Kurim, Czech Republic), see Figure A2B.

A.1.3. | Determination of modulus in cyclic tests

A decay of E can be caused by damage or by viscoelastic creep effects. In a monotonic tensile experiment, this decay cannot be observed. For that purpose, cyclic load–unload experiments can be used. The modulus can be evaluated for each loading cycle, so that the evolution of E throughout the experiment becomes visible. Due to the viscoelastic material response at the start of each cycle, an evaluation of E according to ISO 527 is unreliable, but the curves have a more linear behavior at intermediate stress levels. Therefore, the part of the curve between the data points at 5 and 10 MPa was chosen for evaluation of E, as is shown in Figure A3. For each cycle, the maximum applied strain and the minimum residual strain, $\varepsilon_{\text{appl}}$ and ε_{res}, were evaluated as well. Correlating ε_{res} with $\varepsilon_{\text{appl}}$ of the previous cycle offered additional information on the deformation behavior. Increasing values of ε_{res} indicated the presence of plastic deformation, which was a result of exceeding the flow stress and may have been accompanied by the creation of additional volume. However, the applied forces were greater than zero for the majority of time, so creep behavior was expected too. Additionally, viscoelastic effects and irreversible deformation could not be easily distinguished as source of ε_{res}. Some sources[19] suggest to prestrain the samples and continue characterization after a thorough relaxation period. In this paper, we opt to show the continuous load–unload procedure as well as DMA measurements with prestrain as a discontinuous approach, since both loading profiles could be relevant for specific applications.

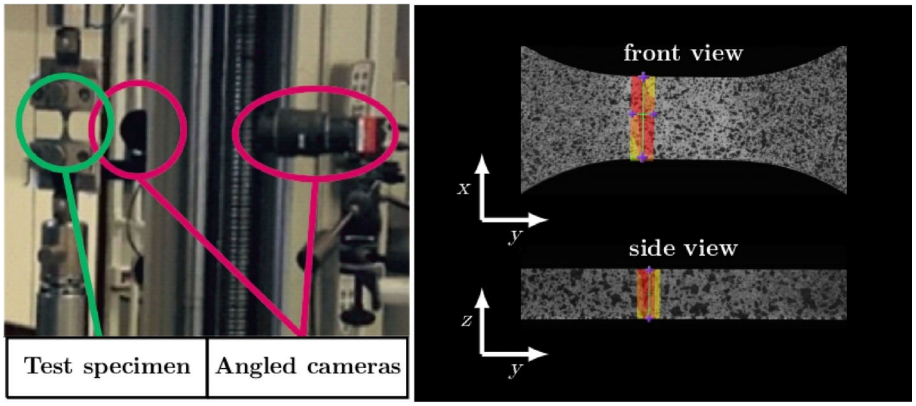

(A) (B)

FIGURE A2 (A) Tensile test setup with two cameras at a 90° angle and (B) surface strain measurement using digital image correlation at highly strained cross sections, with the *y*-direction being the loading direction

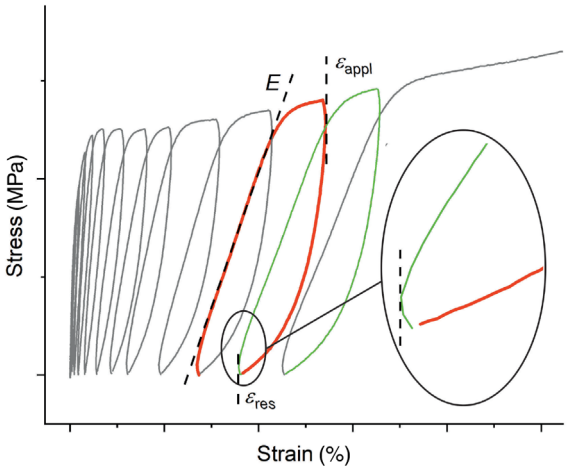

FIGURE A3 Representative stress–strain curve of a cyclic load–unload experiment. The applied strain ε_{appl} and the Young's modulus E are recorded for each cycle as well as the residual strain ε_{res}, which stems from previous loading cycles

A.1.4. | DMA measurements with prestrain

The DMA specimens were loaded on a Zwick Z001 (Zwicke/Roell) with a 1-kN load cell, up to a certain prestrain to gradually induce damage. These prestrains were measured locally on the specimen surface via digital image correlation, as described above. Pneumatic grips were used for the clamping of the specimens. The prestraining was performed at 1 mm/min crosshead speed and room temperature. Although some literature sources suggest complete relaxation as early as 10 min after prestraining,[8] specimens were carefully removed and left to relax for 7 days. Subsequent DMA measurements were performed at room temperature (23°C) at a frequency of 1 Hz using a Modular Compact Rheometer MultiDrive by Anton Paar (Anton Paar, Graz, Austria). The stress amplitude was set to 0.5 MPa in tension, while the mean stress level was 0.75 MPa. This ensured tensile loading throughout the whole experiment. The clamping length for the prestraining and the DMA measurements was 35 mm. The measured storage moduli were interpreted as the material's Young's modulus, E, at different stages of damage, depending on the prestrain. As additional parameter to judge the integrity of the materials, the mechanical loss factor, tan δ, was evaluated as well. This way, prestrains of 0%, 5%, 10%, 15%, 20%, 30%, and 40% were investigated using three specimens per material and level of prestrain. Here, it should be noted again that the values for E and tan δ should primarily be used to compare the two materials in question. A comparison of exact values to other sources in the literature is problematic due to the adapted specimen geometry used in these experiments.

A.1.5. | X-ray computed tomography

A.1.5.1. | Equipment for X-ray computed tomography

Several X-ray computed tomography (CT) scans were performed using a Nanotom 180 NF (GE Phoenix/X-ray, Wunstorf, Germany), equipped with a 180-kV nano-focus X-ray tube and a molybdenum target on a beryllium window. Because the structural resolution by CT is highly dependent on the investigated sample size and the amount of available detector pixels, a multiscale approach according to Plank et al.[34] was followed. To get an overview of a large region of interest, six specimens (PP-B 0%, 20%, 40% and PP-H 0%, 20%, 40%) were scanned at once with an edge length of a volumetric pixel (voxel size) of 16.5 μm^3. With this voxel size, a field of view of approximately 39^3 mm^3 could be investigated at once and structures larger approximately three times the

voxel size can be resolved. These overview scans were carried out at 60-kV tube voltage, 500-ms integration time, and 600 projections within a total measurement time of 30 min. To investigate the three-dimensional material behavior in the micrometer range, high-resolution CT scans with a voxel size of 1.25 μm^3 were performed. These scans were limited to regions with the highest degrees of damage, which were determined in the overview scans. The horizontal amount of detector pixels was extended from 2304 to ~4600 pixels and the virtual detector mode "VSensor 2" was used. This was done to capture the entire cross sections of two specimens (~2.5 × 1.5 mm^2 each) in the field of view of one scan. Applying 50 kV as tube voltage and an integration time of 500 ms for all 1900 projection images resulted in a total measurement time of ~340 min. To verify the recorded microstructures in strained samples, additional high-resolution CT scans in the submicron range were performed on an Easytom 160 (RX Solutions, Chavanod, France). This device was equipped with a 160-kV nanofocus X-ray tube and a LaB6 Filament reaching an X-ray focal spot diameter in the range of 400 nm. As target material, tungsten on a diamond window was used, as well as a 4032 × 2688 Pixel 14-bit CCD camera as imager system. A voxel size of 0.5 μm^3 could be reached without cutting the sample cross section. The field of view within the region of interest spanned 1 × 1 × 1 mm^3 and a tube voltage of 50 kV was used. About 1568 projection images were recorded at 3500 ms integration time, resulting in a total measurement time of 548 min for each scan.

To reconstruct a 3D volume from the recorded 2D projection images, a filtered back projection algorithm (e.g., Feldcamp et al.[35]) implemented in the reconstruction software tools of the abovementioned CT manufacturer was applied.

A.1.5.2. | X-ray tomography data analysis

The CT data analysis was performed using the commercially available software tool, VG Studio MAX 3.4 (Volume Graphics, Germany). This software package includes a porosity/inclusion analysis tool, as well as tools to determine mean gray values of certain defined regions of interest. Segmentation and three-dimensional visualization of the defect structures were done by applying a simple threshold method often used for porosity[36,37] or matrix evaluations[38] in composites. To determine a proper threshold value, a multiscale approach as shown in the study by Kastner et al.[37] is usually used. Most of the times, this leads to sufficient quantitative values, as long as all available microstructures can be resolved by the used voxel resolution. However, the maximum used resolution of 0.5 μm^3 voxel size showed that there are much smaller defects within the investigated specimens. Thus, a reliable quantification of defect volume was not possible using this multiscale approach. To overcome this problem, a rule of mixture was applied on the gray levels of the CT images recorded at 16.5 μm^3 voxel size. The mean gray values of the undamaged specimens are set as a reference density of 0.9 g/cm^3 (data sheet value for both materials) and a density of 0 g/cm^3 is assumed for the surrounding air. By correlating these reference values to the gray levels of the damaged specimens, an estimation of the porosity can be made, assuming that nonvisible cracks and voids lead to a reduction of material density and therefore a linear change in gray level. Weissenbacher[39] demonstrates that a density contrast of 0.1 g/cm^3 can be resolved clearly at 120 kV. By using 60 kV as tube voltage for the investigations, the density contrast between different samples in terms of change in gray values is significantly higher.[40]